Machine learning models for the prediction of energy, forces, and stresses for Platinum

J. Chapman, R. Batra, R. Ramprasad*

Department of Materials Science & Engineering, Georgia Institute of Technology, Atlanta, Georgia

ABSTRACT

Materials properties such as defect diffusion and/or dissociation, mechanical fracture and void nucleation, under extreme temperatures and pressures, are all governed by the interactions between individual and/or groups of atoms. Computational tools have been instrumental in understanding the atomistic properties of materials at these length scales. Over the past few decades, these tools have been dominated by two levels of theory: quantum mechanics (QM) based methods and semi-empirical/classical methods. The former are time-intensive, but accurate and versatile, while the latter methods are fast but are significantly limited in veracity, versatility and transferability. Machine learning (ML) algorithms, in tandem with quantum mechanical methods such as density functional theory, have the potential to bridge the gap between these two chasms due to their (i) low cost, (ii) accuracy, (iii) transferability, and (iv) ability to be iteratively improved. In this work, we prescribe a new paradigm in which potential energy, atomic forces, and stresses are rapidly predicted by independent machine learning models, all while retaining the accuracy of quantum mechanics. This platform has been used to study thermal, vibrational, and diffusive properties of bulk Platinum, highlighting the framework's ability to reliably predict materials properties under dynamic conditions. We then compare our ML framework to both QM, where applicable, and several Embedded Atom Method (EAM) potentials. We conclude this work by reflecting upon the current state of ML in materials science for atomistic simulations.

1. Introduction

Many dynamic phenomena, such as the nucleation of voids, and how a material fractures, aregoverned by individual atomistic processes interacting with one another [1–3]. However, accurately capturing the intricacies of such processes is often non-trivial, owing to the complexity of the interactions, as well as the time and length scales required to accurately study them [4]. Therefore, any strategy that probes the atomic regime, be it experimental or computational, must be capable of capturing the dynamic evolution of atomistic processes.

Historically, computational methods have been employed to study the dynamic evolution of such mechanisms, and have been widely used to explain a plethora of atomsitic processes [5–7]. In particular, two broad classes of computational methodologies have been widely used to study an abundance of materials phenomena: QM based methods, e.g., density functional theory (DFT), and semi-empirical/ classical methods, e.g., EAM [8–13]. While QM provides access to properties with an extremely high level of fidelity, the computational cost of such methods severely restricts the types of problems that can be practically studied. On the other hand, classical methods, such as EAM, have been widely
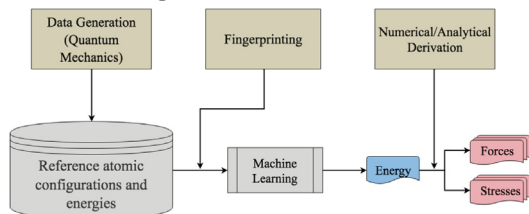
used to study such properties. While these methods have seen success over the years, due to their significant cost reduction when compared to QM methods, they generally break down when making predictions outside of the respective reference data, which is usually aimed at predicting a specific set of properties.

A third pathway, data-driven methods, have recently emerged as a possible suitor whose aim is to bridge the gap between these two extremes [14–22]. Recent progress in the area of machine learning (ML) for atomistic simulations [23–27] have lead to the development of plethora of new models for Al [27–32], Cu [31,33], Ti [31], W [31,34,89], Pd [88], C [31,35,36], Si [31,32,37], Na [32], Mo [38], Fe [39], Zr [40], SiO_2[33]. ML models have a functional form, which is often non-linear in nature, backed by statistics rather than physics. While ML models still suffer from inaccuracies during extrapolations, and are in-fact more likely to fail under such conditions than their classical counterparts, these approaches offer a number of advantages over the fixed-functional forms of empirical models such as the speed required to generate new models, their accuracy when compared to first-principles methods (force and energy prediction errors on the order of 0.05 eV/Å and 10 meV/atom, respectively) [27–31,24–26],

---

* Corresponding author.
  E-mail address: rampi.ramprasad@mse.gatech.edu (R. Ramprasad).

Current ML Methodologies
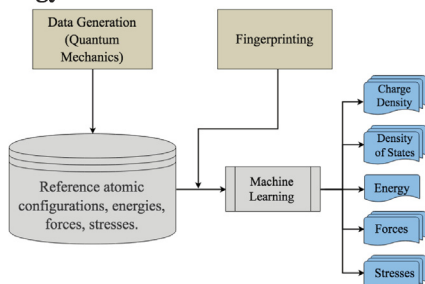

AGNI Methodology

Fig. 1. (Top) General workflow for current ML schemes, in which a single property such as potential energy, is calculated directly via ML, and subsequent properties, such as forces and stresses, are derived from the predicted energy (however, this general workflow can also operate along many different pathways, e.g. learning forces directly and integrating to get the energy) (Bottom) General workflow for our AGNI platform, in which all properties (energies, forces, stresses) are predicted simultaneously via independent ML models.

and their ability to be iteratively improved in a systematic manner [41].

However, the ML methodologies described above have a drawback in that models are generally fit to predict a single property, e.g,. potential energy, while other properties such as forces, stresses, etc, are derived from the first property. This poses a problem, as any errors in the model's primary output will be propagated down to any of the subsequently derived properties [42–48]. To bypass this issue, a new paradigm, henceforth referred to as AGNI, is proposed here to rapidly predict properties such as energy, stresses, and atomic forces, as well as electronic charge density, electronic density of states, etc., as has been demonstrated recently [49], simultaneously through the use of independent ML models. By using independent ML models to learn each desired property, error propagation via derivation/integration cannot occur. Therefore, each ML model can be optimized to obtain a high level of fidelity. Fig. 1 shows a qualitative description of the differences between current ML schemes and the AGNI scheme.

To validate this scheme we have chosen elemental Platinum because of its commercial importance, particularly in the regime of catalysis [50–56], as well as its importance as a bulk material, in part because of its strong mechanical properties and high melting temperature [57–59]. Classical methods have generally struggled to accurately, and universally predict both Pt's surface and bulk properties [60,61]. While less complex properties, such as the cohesive energy, can be accurately reproduced by many semi-empirical models, more complex phenomena such as the activation energy of a single vacancy, are not reliable [61].

To this end, predictions of more complex properties, such as the dissociation of coupled vacancies, void nucleation, and melting, which are governed by the interactions of less complex phenomena [62–64], cannot be universally trusted. Therefore, ML can be employed to fill this void and bring the community closer to bridging the gap between QM methods and experimental observations for Pt.

In this work, a plethora of Pt bulk properties are simulated to showcase the breadth of our three ML models for the direct (and independent) prediction of energy, atomic forces and stresses, given only the atomic configuration. Properties, such as the bulk modulus, vacancy formation energy, and elastic constants, among others, are predicted using all three ML models. Ionic relaxations of highly disordered systems, as well as calculations of phonon frequencies are used to show how our ML models respond to both large and small atomic perturbations. The diffusion of a single vacancy within an otherwise pristine bulk system is considered, along with how entropic effects can help to lower the activation barrier for diffusion. The kinetics of the dissociation and diffusion of a divacancy are simulated via nudged elastic band calculations. Finally, a discussion of the disagreement between several EAM potentials and DFT, for the cases of vacancy diffusion and divacancy dissociation, and how the ML models presented in this work alleviate this difference follows. The collection of atomistic phenomena studied in this work, along with further improvements to the platform itself, lays the groundwork for the future study of more complex properties not explicitly considered in this work, such as the intricate kinetics surrounding non-trivial line and planar defects, as well as the temperature dependence of mechanical properties, none of which can be accurately predicted with current classical methods [61].

2. Computational details

2.1. AGNI workflow

As described earlier [30,41,65], our ML platform consists of several key steps, regardless of the property being predicted: (1) The generation of a diverse set of reference data, (2) Numerically encoding local/structural geometric information (fingerprinting), (3) Training a ML model given some subset of the reference data, (4) Employing the final ML models in an MD engine, capable of simulating the dynamic, time-evolution of atomistic processes. A visual workflow of these steps can be found in the Supplemental information.

2.2. Reference data generation

A comprehensive set of reference data, summarized in Table 1, was prepared for Pt in an accurate and uniform manner in order to minimize numerical noise intrinsic to atomistic calculations. All reference data was obtained using the Vienna Ab initio simulation package (VASP) [66–70]. The Perdew-Burke-Ernzerhof (PBE) functional [71] was used to calculate the electronic exchange-correlation interaction. Projector augmented wave (PAW) potentials [72] and plane-wave basis functions up to a kinetic energy cutoff of 500 eV were used. All projection operators (involved in the calculation of the non-local part of the PAW pseudopotentials) were evaluated in the reciprocal space to ensure

Table 1

Summary of the reference data set that was prepared for Platinum force field generation. The data is divided into subsets based on the type of defect that is present. $T = 0$ K represents NEB calculations, where $T > 0$ K represents MD calculations. Configurations are represented by each atomic configuration present in the data. For the system containing 4 vacancies, the vacancy configurations represent two isolated vacancies and one divacancy in a 108-atom cell (104 total atoms).

Defect Type	Systems	Temperature	# Configurations	# atoms	Phase
Defect-free	Bulk (w/o strain)	300,1000,2000	2500	32	FCC
Defect-free	Bulk (w/strain ± 7 %)	300,1000,2000	3000	32	FCC
Point Defect	Bulk with 1 vacancy	0, 1000, 1500, 2000	5000	255	FCC
Point Defect	Bulk with Divacancy	0, 1000, 1500, 2000	5000	254	FCC
Point Defect	Bulk with 4 vacancies	1000, 1500, 2000	5000	104	FCC

further precision. Monkhorst-Pack [73] **k**-point meshes were carefully calibrated for each atomic configuration to ensure numerical convergence in both energy and atomic forces. For all nudged elastic band (NEB) calculations, the climbing image formalism was employed [70], with ionic relaxations considered converged at an energy difference of 10^{-2} eV, and electronic convergence terminated at an energy difference of 10^{-4} eV.

2.3. Fingerprinting atomic configurations

A hierarchical representation of an atom's local structural environment was created to encode geometric information that maps directly to properties such as the total potential energy, atomic forces, and stresses. This hierarchy aims to capture different aspects of the atomic neighborhood with features resembling scalar, vector, and tensor quantities. The functional forms of all atomic-level fingerprint components are defined as [65]:

$$S_{i;k} = c_k \sum_{j \neq i} \exp\left[-\frac{1}{2}\left(\frac{r_{ij}}{\sigma_k}\right)^2\right] f_{cut}(r_{ij}) \tag{1}$$

$$V_{i,\alpha;k} = c_k \sum_{j \neq i} \frac{r_{ij}^\alpha}{r_{ij}} \exp\left[-\frac{1}{2}\left(\frac{r_{ij}}{\sigma_k}\right)^2\right] f_{cut}(r_{ij}) \tag{2}$$

$$T_{i,\{\alpha,\beta\};k} = c_k \sum_{j \neq i} \frac{r_{ij}^\alpha r_{ij}^\beta}{r_{ij}^2} \exp\left[-\frac{1}{2}\left(\frac{r_{ij}}{\sigma_k}\right)^2\right] f_{cut}(r_{ij}) \tag{3}$$

with r_i and r_j being the Cartesian coordinates of atoms i and j, and $r_{ij} = |\mathbf{r}_j - \mathbf{r}_i|$. α and β represent any of the three x, y, or z directions. The σ_k values control the width of the Gaussian functions, and are determined via a grid-based optimization process [29]. The damping function $f_{cut}(r_{ij}) = \frac{1}{2}[cos(\frac{\pi r_{ij}}{R_{cut}}) + 1]$, smoothly decays towards zero, has a cut-off radius R_{cut} chosen to be 8 Å. c_k is a normalization constant given by $\left(\frac{1}{\sigma_k \sqrt{2\pi}}\right)^3$ (for the force model this normalization constant was set to 1). The pre-factors $\frac{r_{ij}^\alpha}{r_{ij}}$ and $\frac{r_{ij}^\alpha r_{ij}^\beta}{r_{ij}^2}$, which create unique vector and tensor components respectively, help to capture angular information about the local atomic environment by computing all possible dipoles between atomic neighbors, and their interactions in different directions.

This processes of atomic fingerprinting renders the vector and tensor components directionally-dependent, in contrast to the scalar quantity [65]. Therefore, for the case of learning the potential energy, rotationally-invariant forms of these quantities must be created. The invariant form of the vector component is then defined as:

$$V_{i,k} = \sqrt{(V_{i,x;k})^2 + (V_{i,y;k})^2 + (V_{i,z;k})^2} \tag{4}$$

and the invariant forms of the tensor component are:

$$T'_{i,k}$$
$$= T_{i,\{x,x\},k} T_{i,\{y,y\},k} + T_{i,\{x,x\},k} T_{i,\{z,z\},k} + T_{i,\{y,y\},k}$$
$$T_{i,\{z,z\},k} - (T_{i,\{x,y\},k})^2 - (T_{i,\{x,z\},k})^2 - (T_{i,\{y,z\},k})^2 \tag{5}$$

and

$$T''_{i,k} = det(T_{i,\{\alpha,\beta\},k}) \tag{6}$$

2.4. Machine learning

For global properties, such as potential energy, the atomic fingerprints described above are not sufficient, as the they cannot map directly to a global property (only per-atom quantities). Therefore, a second process mapping the atomic fingerprints to a single, structural fingerprint is required [65]. In this work, ML models that learn the potential energy, as well as the stress tensor, employ such a procedure. Table 2 indicates the final forms of all fingerprints for energy, stresses,

Table 2
The final fingerprint forms utilized to learn energy, stresses, or atomic forces. For the property type, the subscripts i and I represent a per-atom or per-structure quantity respectively, and the superscripts α, β represent two possible Cartesian directions. The complete set of optimized σ_k values for each property type can be found in the Supplemental information.

Property Type	# σ_k	σ_k Range (Å)	Final Fingerprint Form
Forces (F_i^α)	8	(1.0, 9.0)	$V_{i,\alpha;k}$
Stresses ($S_I^{\alpha,\beta}$)	20	(1.5, 11.5)	$M^n(\sum_{i=1}^N T_{i,\{\alpha,\beta\};k})$
Energy (E_I)	20	(1.5, 11.5)	$\{M^n(\sum_{i=1}^N S_{i,k}), M^n(\sum_{i=1}^N V_{i,k}), M^n(\sum_{i=1}^N T_{i,k})\}$

and forces. Here the function $M^n(X)$ represents the nth moment of the fingerprint components. For this work only the first ($n = 1$) moment is considered, and can be interpreted as the average atomic environment of the system.

After the final fingerprint forms have been chosen, and a subset of our reference data has been selected, we employ Kernel Ridge Regression (KRR) to create three independent ML models for atomic forces, potential energy, and the stress tensor. This learning scheme employs a similarity-based non-linear kernel to establish a mapping between the reference fingerprints and the desired property using a functional form defined by [27–31]:

$$P_X = \sum_Y \alpha_Y \exp\left[-\frac{1}{2}\left(\frac{d_{XY}}{\sigma}\right)^2\right] \tag{7}$$

Here the summation runs over the number of reference environments, with Y being each fingerprint within a given model's training set. P represents the desired property (total potential energy, stress tensor components, or atomic force components), where X is the fingerprint of the new structure. d_{XY} represents the euclidean distance between fingerprints X and Y in the hyperspace they are defined on, specified by a length scale σ. During the model's training phase, the regression weights α_Y and the length scale σ are determined by optimizing a regularized objective function through a 5-fold cross validation process.

2.5. Other computational details

Three Embedded Atom Method (EAM) potentials, henceforth referred to as EAM-B [57] EAM-Z [58], and EAM-F [59] (due to their respective authors) were chosen for this work and were used as a comparison to the ML models presented in this work. All EAM potentials were chosen for their ability to accurately capture a variety of bulk properties for Pt with respect to experimental evidence. All MD simulations (outside of DFT reference data generation) were performed using the Large-scale Atomic/Molecular Massively Parallel Simulator (LAMMPS) package [74]. Vibrational calculations were performed using the Atomic Simulation Environment (ASE) [75]. This ML scheme has been benchmarked against both EAM and DFT, for the calculation of energy, forces, and stresses, and is approximately 5 orders of magnitude faster than DFT, but roughly 2 orders of magnitude slower than EAM.

3. Results

3.1. ML model statistics

During the training phase of the model creation process, statistical measures are first used to determine if a given model is capable of making reliable predictions. In Fig. 2, several such metrics are provided: (1) the root mean square error (RMSE) as a function of the number of training points, (2) the maximum 1% error as a function of the number of training points, and (3) a parity plot for the best
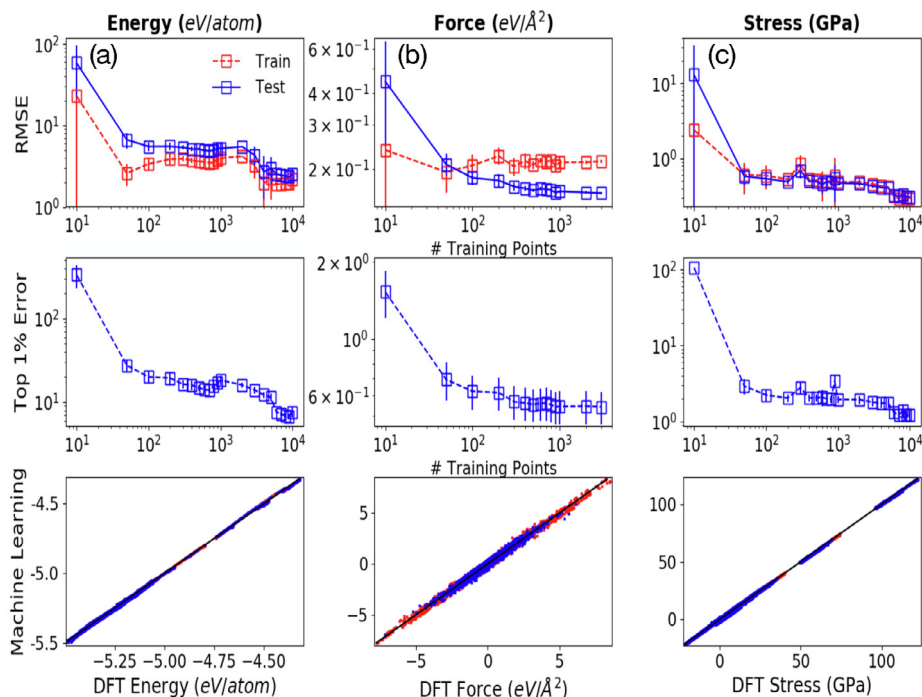
Fig. 2. Statistical error metrics used to compare ML models during the optimization process. The columns are labelled as (a) Energy, (b) Force, (c) Stress. The top row shows the average RMSE of both the training and test sets. The middle row measures the max 1% error of the test set. The x-axis for the top two rows corresponds to the number of training points in a given model. The bottom row shows parity plots of the final model used throughout this work. Column titles indicate the property's units.

generated model. For all three cases, both the overall RMSE, as well as the maximum 1% error, decrease as the training set size increases.

However, saturation occurs in the overall learning for all models by a training set size of 3000 points. All statistical error metrics used for this work for the final ML models can be seen in Table 3. Overall, these metrics indicate that all three ML models can adequately capture their respective DFT reference data over a large range of external conditions. However, such statistical metrics are not the deciding factor when determining if a given model can be used to simulate dynamical material properties. Further validation, as seen in the following sections, must be performed to say that a given ML model can be confidently deployed to study more complex phenomena.

3.2. Thermodynamic properties

The three generated ML models were used to reproduce several thermodynamic quantities, shown in Table 4. We begin this discussion by looking at the predictions made by the ML-energy model. The cohesive energy (E_0), equilibrium volume (V_0), and bulk modulus (B) were all obtained by fitting the Birch-Murnaghan equation of state [76] (EOS) to energies corresponding to volumes between 14 and 17 $\mathring{A}^3$. The cohesive energy and the equilibrium volume were also obtained from a geometry optimization. The bulk modulus, along with upper and lower bounds for the shear modulus (G), as well as the Young's modulus (E), can also be calculated via the Voigt-Reuss-Hill approximation [77].

Table 3
Statistical error metrics of the final ML models, for each property learned, generated in this work. All values presented here are the metrics calculated on a given model's test set. The final row corresponds to the number of training points in the final models chosen for this work.

Error Metric	Energy model (meV/ atom)	Force model (eV/Å)	Stress model (GPa)
RMSE	2.73	0.15	0.42
STD	2.71	0.15	0.41
Max 1% Error	7.90	0.80	1.68
r^2	0.99	0.99	0.99
# Training Points	1728	3000	3000

Table 4
Thermodynamic properties of Pt, calculated using either the ML energy or stress models, and DFT. $*$ represents the Birch-Murnaghan EOS [76], where $\ddagger$ represents the Voigt-Reuss-Hill approximation [77], and $\wp$ represents a geometry optimization. The values in brackets for the shear and Young's modulus represent the calculated lower and upper bounds. For DFT's calculation of the elastic coefficients, two values are reported using different methods: (1) Energy as a function of strain, and (2) Stress as a function of strain (in brackets). Please see text for details on the prescription used to calculate the elastic constants.

Property	DFT	ML-Energy	ML-Stress
E_0 (eV/atom)	$-6.05*$, $-6.05^{\wp}$	$-6.05*$, $-6.05^{\wp}$	–
V_0 ($\mathring{A}^3$/atom)	$15.68*$, $15.73^{\wp}$	$15.69*$, $15.74^{\wp}$	–
B (GPa)	$265.62*$, $227.39\ddagger$	$265.95*$, $239.86\ddagger$	$234.39\ddagger$
G (GPa)	$[76.51\ddagger$, $77.08\ddagger]$	$[80.91\ddagger$, $81.48\ddagger]$	$[76.22\ddagger$, $76.85\ddagger]$
E (GPa)	$[206.38\ddagger$, $207.76\ddagger]$	$[218.19\ddagger$, $219.57\ddagger]$	$[206.29\ddagger$, $207.83\ddagger]$
C_{11} (GPa)	341.12 (341.36)	359.83	348.46
C_{12} (GPa)	170.53 (179.07)	179.88	177.36
C_{44} (GPa)	71.61 (65.32)	75.83	71.06
E_{1f} (eV)	0.65	0.55	–
E_{2b} (eV)	-0.18	-0.15	–

Employing both the Birch-Murnaghan EOS and the Voigt-Reuss-Hill approximation allows one to compare the agreement between the ML energy and stress values. The elastic constants C_{11}, C_{44}, and C_{12} were calculated according to a prescription described by Ding et al. [78]. Fig. 3 shows energy and stress as a function of strain for the several types of strain used in this work. It can seen that the ML-energy model reproduces DFT with exceptional accuracy.

The elastic properties mentioned above can also be calculated with the ML-stress model. For the case of the bulk, shear, and Young's modulus, the Voigt-Reuss-Hill approximation was used, as this ML model only has access to stress. The elastic constants were calculated according to $\sigma_{ii} = C_{ii} \, \epsilon_{ii}$, where σ_{ii} is the stress. The agreement across multiple, unique approximation methods can be seen between not only the ML-energy and ML-stress models, but also between the ML-stress model and DFT. This agreement shows that both models can be used interchangeably to reliably make predictions of a material's mechanical properties.

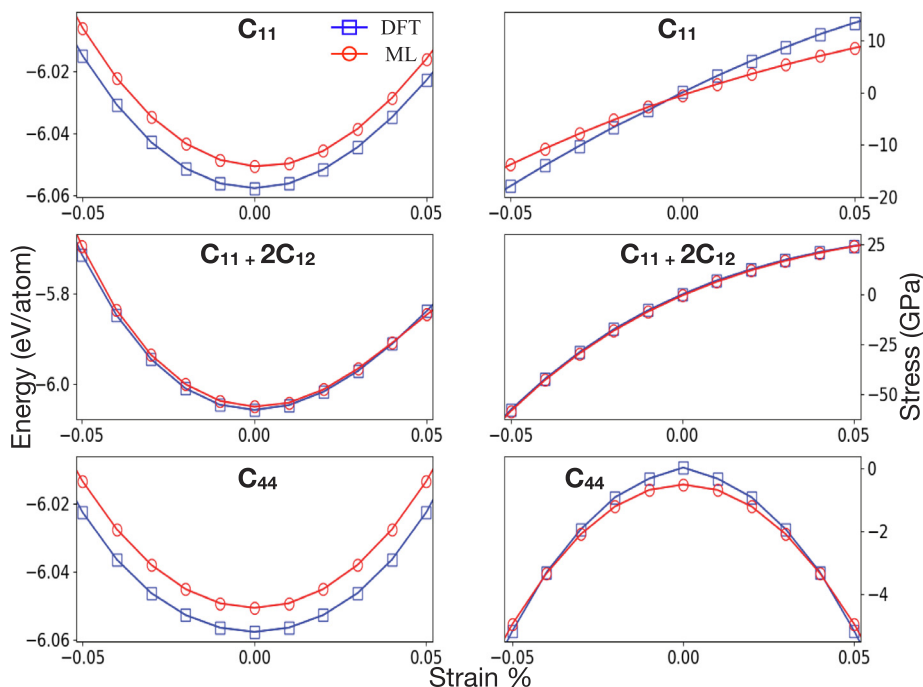For the case of the single vacancy formation energy (E_{1f}), and the

Fig. 3. Comparison of different elastic constants as computed using DFT and ML models, as derived using the energy vs strain trends (first column) and stress vs strain trends (second column). Please see text for more details.
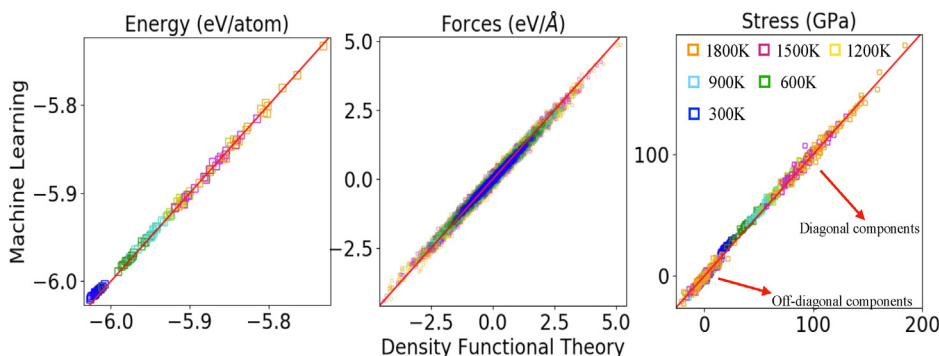

Fig. 4. ML model predictions, compared against DFT for (a) force, (b) stress, (c) energy. Structures were gathered from trajectories of defect-free bulk Pt at different temperatures, generated during MD using the ML-force model. It should be noted that the configurations encountered during these MD simulations are not explicitly present in the model's training set. Colors correspond to the different temperatures used.

divacancy binding energy (E_{2b}), both the ML force and energy models were employed. The binding energy is calculated as the difference in energy between the two vacancies adjacent to one another, and the two vacancies being separated by several intermediate sites. For this, two vacancies were placed next to each other, and NEB calculations were performed (which will be explained in detail in later sections), allowing for one of the vacancies to move away from the other. At some distance away, each vacancy effectively acts as a single vacancy, and no longer feels the effect of the other. Forces and energies, calculated by each of their respective ML models, were used to relax the corresponding structures.

The vibrational density of states (VDOS) as well the phonon band structure, calculated via the finite displacement method [79], which have to be properly represented to allow for the prediction of thermodynamic quantities such as thermal expansion, heat capacity, etc, are used to determine the ML force model's capability of capturing small atomic perturbations. The ML-force model shows good agreement with respect to DFT for predicting the acoustic modes of the phonon band structure, indicating that under small atomic perturbations (as opposed to the much larger displacements often encountered during dynamic trajectories), the fidelity of the force model is maintained. This also implies that any properties one desires to extract from the phonon frequencies, e.g,. heat capacity, vibrational density of states, etc, can be

reliably obtained as well. Figures regarding the vibrational analysis performed here can be found in the Supplemental information.

3.3. Dynamic properties

The ML model's performance during dynamic conditions is of great importance, as the complex materials phenomena that we aim to capture often occur under these conditions. To this end, we consider MD simulations of a 256-atom bulk configuration. Canonical ensemble MD was performed at several temperatures between 300 and 1800 K. A timestep of 0.5 fs was chosen with a total simulation time of 10 ns. Single-step DFT calculations were also performed on several snapshots, randomly chosen from each trajectory, to verify the accuracy of the models. Parity plots comparing the forces, stresses, and energies, predicted by DFT and each corresponding ML model, on these snapshots are shown in Fig. 4. The excellent agreement between the ML models and DFT indicates that all three ML models can make accurate predictions within configuration spaces not explicitly employed in their respective training sets. Similar results were obtained when an identical analysis was performed on systems containing a single vacancy, and can be found in the Supplemental information.

3.4. Vacancy kinetics

The ML model's ability to extrapolate during dynamic conditions gives rise to another question: can the ML models accurately predict the kinetics of specific atomistic processes with the accuracy of QM? A straightforward approach to answer this question is to perform an ionic relaxation starting from a highly disordered state. To this end, we employ the ML-force and ML-energy models to perform ionic relaxations on highly disordered systems, starting from initial configurations of: (1) defect-free bulk, (2) bulk with a single vacancy, and (3) bulk with a divacancy, in a $7 \times 7 \times 7$ supercell. Random displacements on these configurations of up to 0.5 Å, in each of the x, y, and z cartesian directions, were used. Each relaxation was terminated when an accuracy of 10^{-7} eV and 10^{-2} eV/Å, for energies and forces respectively, was reached. Several runs were performed with varying random displacement seeds to ensure the fidelity of the model under different disordered configurations. All three scenarios show excellent agreement with their respective equilibrium geometries. A video of all optimizations can be found in the Supplemental section.

Next, we consider the pathway of a single vacancy hopping from one site to a nearest-neighbor site in a bulk fcc configuration. NEB calculations, performed with the ML energy and force models (as well as all three EAM potentials and DFT), along with the climbing image formalism, were used to determine the minimum energy pathway (MEP) of the hop. Fig. 5(left) shows the MEP predicted by ML as well as DFT. For the case of ML, the diffusion barrier was predicted to be 1.20 eV, which is in excellent agreement with the calculated DFT value of 1.19 eV. EAM-B, EAM-F, and EAM-Z predict barrier heights of 0.83, 0.81, and 0.54 eV respectively. Experimental values vary depending on vacancy concentration and quench rates[80–82], however, the values reported are typically between 1.0 and 1.4 eV. Many factors can contribute to the accuracy of the calculated DFT barrier, including the treatment of surface effects around the vacancy [83], as well as the cell size's possible restriction of relaxations [84]. However, one should be reminded that the ML models can only be as accurate as the reference data used to train them, and therefore should only be compared to the DFT value, and not experimental values.

The activation energy predicted by the NEB calculations can also be determined through dynamic simulations. In this case, MD runs were performed on a $7 \times 7 \times 7$ supercell containing 1371 atoms and a vacancy, between 1000 K and 2000 K, using the ML-force model to drive the dynamics. Simulations were run for a minimum of 1 ns (with a time step of 0.5 fs), but were extended for lower temperatures to ensure statistical diversity with regards to the hop rates. By observing the

dynamics of the vacancy, the average rate constant (k) for the diffusion process was calculated. k is represented as $\frac{1}{t_{hop}}$, where t_{hop} is the average time taken for a vacancy to migrate from one arbitrary site to an adjacent site. A minimum of 25 hops were recorded at each temperature to ensure that t_{hop} was not dominated by events 2σ or greater away from the mean. Fig. 5(right) shows an Arrhenius plot of k versus the reciprocal temperature.

The ML force model predicts an activation energy of 0.94 eV. As one cannot obtain a dynamic activation energy from DFT, the value of 1.19 eV, determined from the 0 K NEB calculation described earlier, is used and agrees well with the dynamic ML result. While the predicted ML barrier is slightly lower, when compared to the NEB barriers (for both ML and DFT), one can expect that the activation energy obtained through MD will be lower than that obtained through NEB calculations, as such a methodology neglects any entropic effects that may help to "soften" the barrier [85,86]. EAM-B, EAM-F, and EAM-Z predict activation energies of 0.96, 0.94, and 0.63 eV respectively, and is in good agreement with their respective NEB energy barriers, indicating little difference between the static and dynamic cases.

How vacancies interact with one another is also of importance. Here we consider the diffusion/dissociation of a divacancy pair through NEB calculations, using the ML force and energy models, along several possible diffusion pathways. For this, a 4x4x4 FCC supercell containing 254 atoms and a divacancy was considered. Fig. 6 highlights two possible pathways that can occur during dissociation. From these minimum energy pathways (MEP) we can conclude several important pieces of information. The first pertains to the relative thermodynamic stability of the divacancy versus two isolated vacancies. Both ML and DFT predict the divacancy configuration to be higher in energy than that of two isolated vacancies, (this can be seen by observing the difference in energy between the reaction coordinates 0 and 3, as well as 0 and 5, in Fig. 6). The second belongs to the kinetics of the dissociation/diffusion process. When travelling along the ⟨110⟩ direction (from reaction coordinate 0 to 3), the barrier heights between each reaction coordinate remain consistent, with a decrease in energy of the final configuration (as mentioned previously). However, due to the prohibitively large barrier height when travelling from reaction coordinate 4 to 5, one can make the assumption that, under dynamic conditions, diffusion should occur more frequently along the ⟨110⟩ direction.

However, for all three EAM potentials considered in this work, the divacancy is predicted to be more energetically favorable than 2 isolated vacancies, regardless of the diffusion pathway that is chosen. The barrier heights are also predicted to be significantly lower than those calculated by both ML and DFT, indicating a more diffuse solid. The
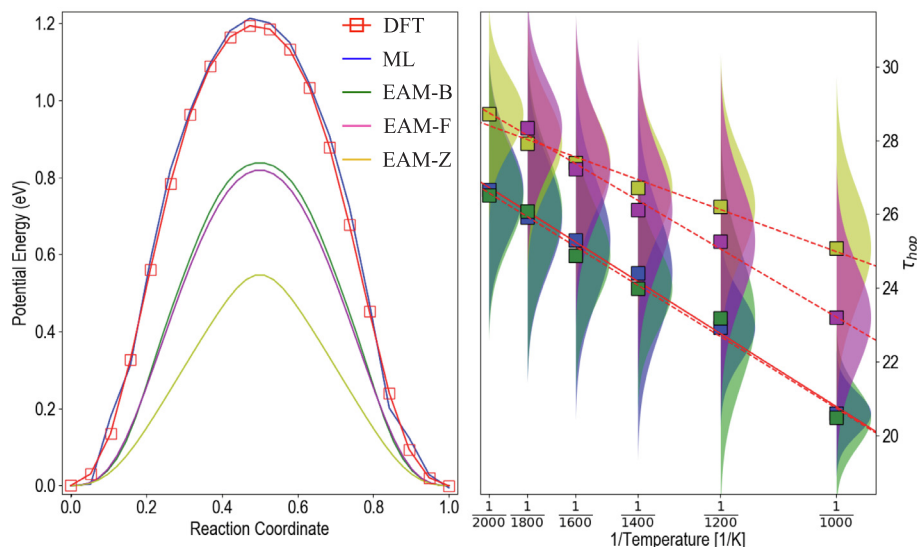

Fig. 5. (left) Nudged elastic band prediction of a single vacancy migrating in bulk Pt. (right) Arrhenius plots for a single vacancy migrating in bulk Pt, generated from all methods used in this work. For each temperature, the MD simulation time was extended so as to allow at least 25 hopping events (thus allowing estimation of an average hop rate, and the corresponding distribution. A linear fit (red lines) was used to determine the dynamic activation energy (Ea).
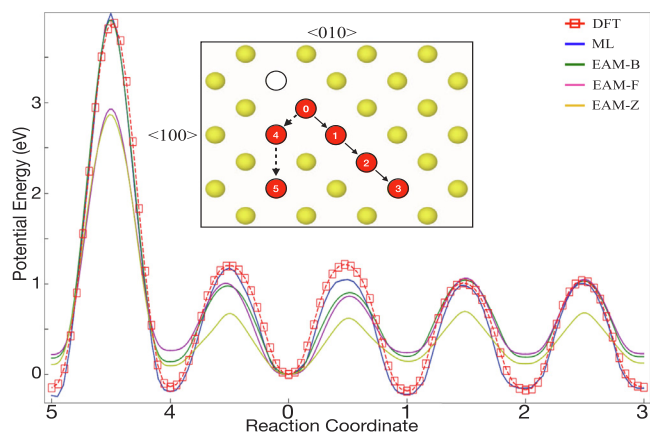
Fig. 6. Nudged elastic band prediction of divacancy migration in bulk Pt. Reaction coordinates correspond to different positions of one vacancy as it moves away from its divacancy pair. As the pathway traverses from (0,1,2,3), one vacancy moves along the $\langle 110 \rangle$ direction away from the other vacancy. As the pathway moves from (0,4,5), one vacancy first moves along a $\langle 110 \rangle$ vector away from the other vacancy. After one hop along $\langle 110 \rangle$, it then moves along a $\langle 100 \rangle$ vector away from the other vacancy. In all scenarios the first vacancy remains stationary. The inserted diagram outlines this procedure, where the white outlined circle represents the stationary vacancy, and light-red circles represent the different end-points of the second vacancy as it moves along each diffusion pathway (numbers in the inserted diagram correspond to the reaction coordinate values along the x-axis of the main plot). All energies plotted refer to the configuration at reaction coordinate 0 as the reference.

differing profiles presented here paint vastly different pictures of vacancy behavior, at least at 0 K. DFT and ML do not seem to favor divacancy formation, indicating that energy must be provided to the system to allow for vacancies to come together. All considered EAM potentials indicate the opposite, in that energy must be supplied to the system to favor vacancy separation. However, we must remind the reader that this picture exists at T = 0 K, and how this portrayal changes at T > 0 K is yet to be fully understood computationally.

At this point there is a critical aspect to all ML schemes that must be discussed: the accuracy of the underlying reference data used to train ML models. As ML methods begin to outperform existing methods, they will be increasingly used to study unexplained phenomena. The accuracy of the reference data used to train the ML models will therefore become an important factor, as the level of theory used to create the reference data must be capable of accurately representing the problem being studied.

For the case of this work, the PBE exchange correlation functional was used to predict properties such as vacancy dynamics. It is well-known that the PBE functional underestimates surface-related properties due to its under-prediction of the electron density around such regions [87]. Therefore, properties such as the vacancy formation/activation energy will be underestimated with respect to experiments. As the DFT reference data is inaccurate, the corresponding ML potential will follow its respective trends. Therefore, as the community progresses further into unknown territory, great care must be taken to ensure the accuracy of the model's reference data, under the conditions being studied, and will ultimately require the use of more accurate, and more computationally demanding, exchange correlation functionals.

4. Conclusion

In this work, a new machine learning scheme, designed to circumvent the computational cost of QM-based methods such as DFT, while retaining their accuracy, has been proposed. Here, we further extend the scope of current ML paradigms by incorporating the predictions of atomic forces, stresses, and potential energy simultaneously and

seamlessly through three independent ML models. This paradigm bypasses the primary drawback of many prominent ML strategies by independently learning all predicted atomic-level properties. The various ML models were validated by accurately reproducing bulk thermal, vibrational, elastic, and diffusive properties of bulk Platinum, with and without the presence of vacancies. In particular, we highlight the ability of the ML models to accurately predict properties such as the activation energy required for a single vacancy to diffuse in bulk, and the kinetics of divacancy dissociation/diffusion, as the EAM potentials used in this work deviate significantly with respect to DFT.

More complex phenomena, such as how the mechanical properties behave as a function of temperature, and the diffusive properties of vacancies in the presence of planar defects, can be examined further, as such properties are relevant not only because of their physical importance, but also because modern classical methods fail to accurately explain them. Due to the nature of ML, the reference data which examines such behavior can be iteratively added to the models presented here, thus improving their predictive power. Using ML to obtain high fidelity atomic-level materials properties, at a fraction of the cost of QM methods, has already made significant progress to studying materials and chemical phenomena, and such strategies will become essential in pushing the boundaries of atomistic materials simulations.

Data availability

The raw data required to reproduce these findings are available to download from https://khazana.gatech.edu. The processed data required to reproduce these findings are available to download from https://khazana.gatech.edu. The force model generated from this work will be made available from the latest public branch of LAMMPS, and all ML models developed in this work will be made available through our web platform (located at https://agni-web.herokuapp.com).

CRediT authorship contribution statement

J. Chapman: Conceptualization, Methodology, Software, Validation, Formal analysis, Data curation, Writing - original draft, Writing - review & editing, Visualization. **R. Batra:** Conceptualization, Software, Validation, Visualization, Visualization, Writing - original draft, Writing - review & editing. **R. Ramprasad:** Conceptualization, Supervision, Writing - original draft, Writing - review & editing, Funding acquisition.

Acknowledgement

Appendix A. Supplementary data

Supplementary data associated with this article can be found, in the online version, at https://doi.org/10.1016/j.commatsci.2019.109483.

References

[1] J.K. Nørskov, F. Abild-Pedersen, F. Studt, T. Bligaard, Density functional theory in surface chemistry and catalysis, Proc. Natl. Acad. Sci. 108 (3) (2011) 937–943, https://doi.org/10.1073/pnas.1006652108 arXiv: https://www.pnas.org/content/108/3/937.full.pdf , https://www.pnas.org/content/108/3/937.

[2] C. Guillaume, E. Gregoryanz, O. Degtyareva, M. McMahon, M. Hanfland, S. Evans, M. Guthrie, S. Sinogeikin, H. Mao, Cold melting and solid structures of dense lithium, Nat. Phys. 7.

[3] M. Buehler, Atomic Modeling of Materials Failure, 2008.

[4] A.J. Cohen, P. Mori-Sánchez, W. Yang, Insights into current limitations of density functional theory, Science 321 (5890) (2008) 792–794, https://doi.org/10.1126/science.1158722 arXiv: https://science.sciencemag.org/content/321/5890/792.full.pdf , https://science.sciencemag.org/content/321/5890/792.

[5] R.O. Jones, Density functional theory: its origins, rise to prominence, and future, Rev. Mod. Phys. 87 (2015) 897–923.

[6] P. Hohenberg, W. Kohn, Inhomogeneous electron gas, Phys. Rev. 136 (1964) B864–B871.

[7] L. Kohn, W. Sham, Self-consistent equations including exchange and correlation effects, Phys. Rev. 140 (1965) A1133–A1138.

[8] J.E. Jones, S. Chapman, On the determination of molecular fields, Proc. R. Soc. Lond. A 106 (1924) 463–477.

[9] M.S. Daw, M.I. Baskes, Embedded-atom method: derivation and application to impurities, surfaces, and other defects in metals, Phys. Rev. B 29 (1984) 6443–6453.

[10] M.S. Daw, S.M. Foiles, M.I. Baskes, The embedded-atom method: a review of theory and applications, Mater. Sci. Rep. 9 (1993) 251–310.

[11] J. Tersoff, New empirical approach for the structure and energy of covalent systems, Phys. Rev. B 37 (1998) 6991–7000.

[12] M.Z. Bazant, E. Kaxiras, J.F. Justo, Environment-dependent interatomic potential for bulk silicon, Phys. Rev. B 56 (1997) 8542–8552.

[13] A.C.T. van Duin, S. Dasgupta, F. Lorant, W.A. Goddard, Reaxff: a reactive force field for hydrocarbons, J. Phys. Chem. A 105 (2001) 9396–9409.

[14] J. Gasteiger, J. Zupan, Neural networks in chemistry, Angew. Chem. Int. Ed. 32 (1993) 503–527.

[15] B.G. Sumpter, C. Getino, D.W. Noid, Theory and applications of neural computing in chemical science, Annu. Rev. Phys. Chem. 45 (1994) 439–481.

[16] K. Rajan, Materials informatics, Mater. Today 8 (2005) 38–45.

[17] R. Ramprasad, R. Batra, G. Pilania, A. Mannodi-Kanakkithodi, C. Kim, Machine learning and materials informatics: recent applications and prospects, npj Comput. Mater. 54.

[18] A. Mannodi-Kanakkithodi, A. Chandrasekaran, C. Kim, T.D. Huan, G. Pilania, V. Botu, R. Ramprasad, Scoping the polymer genome: a roadmap for rational polymer dielectrics design and beyond, Mater. Today 21 (2017) 785–796.

[19] C. Kim, A. Chandrasekaran, T.D. Huan, D. Das, R. Ramprasad, Polymer genome: a data-powered polymer informatics platform for property predictions, J. Phys. Chem. C 122 (2018) 17575–17585.

[20] G. Pilania, C. Wang, X. Jiang, S. Rajasekaran, R. Ramprasad, Accelerating materials property predictions using machine learning, Sci. Rep. 3 (2018) 2810.

[21] T.D. Huan, A. Mannodi-Kanakkithodi, R. Ramprasad, Accelerated materials property predictions and design using motif-based fingerprints, Phys. Rev. B 92.

[22] A. Mannodi-Kanakkithodi, G. Pilania, T.D. Huan, T. Lookman, R. Ramprasad, Machine learning strategy for the accelerated design of polymer dielectrics, Sci. Rep. 6 (2016) 20952.

[23] J. Behler, Machine learning potentials for atomistic simulations, J. Chem. Phys. 145 (2016) 170901.

[24] J. Behler, M. Parrinello, Generalized neural-network representation of high-dimensional potential-energy surfaces, Phys. Rev. Lett. 98 (2007) 146401.

[25] A.P. Bartk, G. Csnyi, Gaussian approximation potentials: a brief tutorial introduction, Int. J. Quant. Chem. 115 (2015) 1051–1057.

[26] S. Chmiela, A. Tkatchenko, H.E. Sauceda, T. Poltavsky, K.T. Schutt, K.R. Muller, Machine learning of accurate energy-conserving molecular force fields, Sci. Adv. 3 (2017) e1603015.

[27] V. Botu, R. Ramprasad, Adaptive machine learning framework to accelerate ab initio molecular dynamics, Int. J. Quant. Chem. 115 (2015) 1074–1083.

[28] V. Botu, R. Ramprasad, Learning scheme to predict atomic forces and accelerate materials simulations, Phys. Rev. B 92 (2015) 094306.

[29] V. Botu, R. Batra, J. Chapman, R. Ramprasad, Machine learning force fields: construction, validation, and outlook, Jour. Phys. Chem. C 121 (2017) 511–522.

[30] V. Botu, J. Chapman, R. Ramprasad, A study of adatom ripening on an al (111) surface with machine learning force fields, Comp. Mater. Sci. 129 (2016) 332–335.

[31] T.D. Huan, R. Batra, J. Chapman, S. Krishnan, L. Chen, R. Ramprasad, A universal strategy for the creation of machine learning based atomistic force fields, npj Comput. Mater. 3 (2017) 37.

[32] N. Kuritz, G. Gordon, A. Natan, Size and temperature transferability of direct and local deep neural networks for atomic forces, Phys. Rev. B 98 (2018) 094109.

[33] W. Li, Y. Ando, Construction of accurate machine learning force fields for copper and silicon dioxide, arXiv:1807.02042.

[34] W.J. Szlachta, A.P. Bartk, G. Csnyi, Accuracy and transferability of gaussian approximation potential models for tungsten, Phys. Rev. B 90 (2014) 104108.

[35] P. Rowe, G. Csnyi, D. Alf, A. Michaelides, Development of a machine learning potential for graphene, Phys. Rev. B 97 (2018) 054303.

[36] V.L. Deringer, G. Csnyi, Machine learning based interatomic potential for amorphous carbon, Phys. Rev. B 95 (2017) 094203.

[37] T. Suzuki, R. Tamura, T. Miyazaki, Machine learning for atomic forces in a crystalline solid: transferability to various temperatures, Int. J. Quant. Chem 117 (2017) 33–39.

[38] C. Chen, Z. Deng, R. Tran, H. Tang, I.-H. Chu, S.P. Ong, Accurate force field for molybdenum by machine learning large materials data, Phys. Rev. Mater. 1 (2017) 043603.

[39] D. Dragoni, T.D. Daff, G. Csnyi, N. Marzari, Achieving dft accuracy with a machine-learning interatomic potential: thermomechanics and defects in bcc ferromagnetic iron, Phys. Rev. Mater. 2 (2018) 013808.

[40] H. Zong, G. Pilania, X. Ding, G.J. Ackland, T. Lookman, Developing an interatomic potential for martensitic phase transformations in zirconium by machine learning, npj Comput. Mater. 4 (2018) 48.

[41] T.D. Huan, R. Batra, J. Chapman, C. Kim, A. Chandrasekaran, R. Ramprasad, Iterative-learning strategy for the development of application-specific atomistic force fields, J. Phys. Chem. C 123 (34) (2019) 20715–20722, https://doi.org/10.1021/acs.jpcc.9b04207.

[42] S. Chmiela, A. Tkatchenko, H.E. Sauceda, I. Poltavsky, K.T. Schütt, K.-R. Müller, Machine learning of accurate energy-conserving molecular force fields 3 (5).

[43] L. Li, J.C. Snyder, I.M. Pelaschier, J. Huang, U.-N. Niranjan, P. Duncan, M. Rupp, K.-R. Müller, K. Burke, Understanding machine-learned density functionals, Int. J. Quantum Chem. 116 (11) (2016) 819–833, https://doi.org/10.1002/qua.25040 arXiv: https://onlinelibrary.wiley.com/doi/pdf/10.1002/qua.25040.

[44] J.C. Snyder, M. Rupp, K. Hansen, K.-R. Müller, K. Burke, Finding density functionals with machine learning, Phys. Rev. Lett. 108 (2012) 253002, , https://doi.org/10.1103/PhysRevLett.108.253002 URL: https://link.aps.org/doi/10.1103/PhysRevLett.108.253002.

[45] A.S. Christensen, F.A. Faber, O.A. von Lilienfeld, Operators in quantum machine learning: response properties in chemical space, J. Chem. Phys. 150(6) (2019) 064105.https://doi.org/10.1063/1.5053562.https://doi.org/10.1063/1.5053562.

[46] A. Khorshidi, A.A. Peterson, Amp: a modular approach to machine learning in atomistic simulations, Comput. Phys. Commun. 207 (2016) 310–324, https://doi.org/10.1016/j.cpc.2016.05.010 URl: http://www.sciencedirect.com/science/article/pii/S0010465516301266.

[47] A.A. Peterson, R. Christensen, A. Khorshidi, Addressing uncertainty in atomistic machine learning, Phys. Chem. Chem. Phys. 19 (2017) 10978–10985, https://doi.org/10.1039/C7CP00375G.

[48] S. Dick, M. Fernandez-Serra, Learning from the density to correct total energy and forces in first principle simulations, J. Chem. Phys. 151 (14) (2019) 144102, https://doi.org/10.1063/1.5114618 arXiv: https://doi.org/10.1063/1.5114618.

[49] A. Chandrasekaran, D. Kamal, R. Batra, C. Kim, L. Chen, R. Ramprasad, Solving the electronic structure problem with machine learning, npj Comput. Mater. 5 (1) (2019) 22, https://doi.org/10.1038/s41524-019-0162-7.

[50] A. Seplveda-Escribano, F. Coloma, F. Rodrguez-Reinoso, Platinum catalysts supported on carbon blacks with different surface chemical properties, Appl. Catal. A: Gen. 173 (2) (1998) 247–257, https://doi.org/10.1016/S0926-860X(98)00183-5 URL: http://www.sciencedirect.com/science/article/pii/S0926860X98001835.

[51] A. Chen, P. Holt-Hindle, Platinum-based nanostructured materials: synthesis, properties, and applications, Chem. Rev. 110 (6) (2010) 3767–3804, https://doi.org/10.1021/cr9003902 pMID: 20170127, arXiv: https://doi.org/10.1021/cr9003902.

[52] S. Zhang, X.-Z. Yuan, J.N.C. Hin, H. Wang, K.A. Friedrich, M. Schulze, A review of platinum-based catalyst layer degradation in proton exchange membrane fuel cells, J. Power Sources 194 (2) (2009) 588–600, https://doi.org/10.1016/j.jpowsour.2009.06.073 URL: http://www.sciencedirect.com/science/article/pii/S037877530901146X.

[53] H. Yang, Platinum-based electrocatalysts with core-shell nanostructures, Angewandte Chemie International Edition 50 (12) (2011) 2674–2676, https://doi.org/10.1002/anie.201005868 arXiv: https://onlinelibrary.wiley.com/doi/pdf/10.1002/anie.201005868.

[54] A. Baiker, Progress in asymmetric heterogeneous catalysis: design of novel chirally modified platinum metal catalysts1communication presented at the first francqui colloquium, brussels, 19–20 february 1996.1, J. Mol. Catal. A: Chem. 115 (3) (1997) 473–493, https://doi.org/10.1016/S1381-1169(96)00352-4 URL: http://www.sciencedirect.com/science/article/pii/S1381116996003524.

[55] N. Tian, Z.-Y. Zhou, S.-G. Sun, Platinum metal catalysts of high-index surfaces: from single-crystal planes to electrochemically shape-controlled nanoparticles, J. Phys. Chem. C 112 (50) (2008) 19801–19817, https://doi.org/10.1021/jp804051e arXiv: https://doi.org/10.1021/jp804051e.

[56] T. Mallat, A. Baiker, Oxidation of alcohols with molecular oxygen on platinum metal catalysts in aqueous solutions, Catal. Today 19 (2) (1994) 247–283, https://doi.org/10.1016/0920-5861(94)80187-8 URL: http://www.sciencedirect.com/science/article/pii/0920586194801878.

[57] C.J. O'Brien, C.M. Barr, P.M. Price, K. Hattar, S.M. Foiles, Grain boundary phase transformations in ptau and relevance to thermal stabilization of bulk nanocrystalline metals, Jour. of Mat. Sci. 53 (2018) 2911–2927.

[58] X.W. Zhou, R.A. Johnson, H.N.G. Wadley, Misfit-energy-increasing dislocations in vapor-deposited cofe-nife multilayers, Phys. Rev. B 60 (2004) 144113.

[59] S.M. Foiles, M.I. Baskes, M.S. Daw, Embedded-atom-method functions for the fcc metals cu, ag, au, ni, pd, pt, and their alloys, Phys. Rev. B 59 (1999) 11693.

[60] G. Grochola, S.P. Russo, I.K. Snook, On fitting a gold embedded atom method potential using the force matching method, J. Chem. Phys. 123 (20) (2005) 204719, https://doi.org/10.1063/1.2124667 arXiv: https://doi.org/10.1063/1.2124667.

[61] S.M. Rassoulinejad-Mousavi, Y. Zhang, Interatomic potentials transferability for molecular simulations: a comparative study for platinum, gold and silver, Sci. Rep. 8 (2018) 2424.

[62] G. Ho, M.T. Ong, K.J. Caspersen, E.A. Carter, Energetics and kinetics of vacancy diffusion and aggregation in shocked aluminium via orbital-free density functional theory, Phys. Chem. Chem. Phys. 9 (2007) 4951–4966, https://doi.org/10.1039/B705455F.

[63] A. Kuksin, G. Norman, V. Stegailov, A. Yanilkin, P. Zhilyaev, Dynamic fracture kinetics, influence of temperature and microstructure in the atomistic model of aluminum, Int. J. Fract. 162 (1) (2010) 127–136, https://doi.org/10.1007/s10704-009-9424-6.

[64] L.V. Zhigilei, Z. Lin, D.S. Ivanov, Atomistic modeling of short pulse laser ablation of metals: connections between melting, spallation, and phase explosion, J. Phys. Chem. C 113 (27) (2009) 11892–11906, https://doi.org/10.1021/jp902294m arXiv: https://doi.org/10.1021/jp902294m.

[65] R. Batra, H.D. Tran, C. Kim, J. Chapman, L. Chen, A. Chandrasekaran, R. Ramprasad, General atomic neighborhood fingerprint for machine learning-based methods, J. Phys. Chem. C 123 (25) (2019) 15859–15866, https://doi.org/10.1021/acs.jpcc.9b03925 arXiv: https://doi.org/10.1021/acs.jpcc.9b03925.

[66] G. Kresse, J. Furthmüller, Efficient iterative schemes for ab initio total energy calculations using a plane-wave basis set, Phys. Rev. B 54.

[67] G. Kresse, D. Joubert, From ultrasoft pseudopotentials to the projector augmented wave method, Phys. Rev. B, 59.

[68] H. Jònsson, G. Mills, K.W. Jacobsen, Nudged elastic band method for finding minimum energy paths of transitions, Classical and Quantum Dynamics in Condensed Phase Simulations 50 (1998) 385.

[69] H. Jònsson, G. Henkelman, Improved tangent estimate in the nudged elastic band method for finding minimum energy paths and saddle points, J. Chem. Phys 113.

[70] H. Jònsson, G. Henkelman, B. Uberuaga, A climbing image nudged elastic band method for finding saddle points and minimum energy paths, J. Chem. Phys 113.

[71] J.P. Perdew, K. Burke, Y. Wang, Generalized gradient approximation for the exchange-correlation hole of a many electron system, Phys. Rev. B 54.

[72] P.E. Blöchl, Projector augmented wave method, Phys. Rev. B 50.

[73] H.J. Monkhorst, J.D. Pack, Special points for brillouin-zone integrations, Phys. Rev. B 13 (1976) 5188.

[74] S. Plimpton, Fast parallel algorithms for short-range molecular dynamics, J. Compu. Phys. 117 (1) (1995) 1–19, https://doi.org/10.1006/jcph.1995.1039. http://lammps.sandia.gov/.

[75] A.H. Larsen, J.J. Mortensen, J. Blomqvist, I.E. Castelli, R. Christensen, M. Duak, J. Friis, M.N. Groves, B. Hammer, C. Hargus, E.D. Hermes, P.C. Jennings, P.B. Jensen, J. Kermode, J.R. Kitchin, E.L. Kolsbjerg, J. Kubal, K. Kaasbjerg, S. Lysgaard, J.B. Maronsson, T. Maxson, T. Olsen, L. Pastewka, A. Peterson, C. Rostgaard, J. Schitz, O. Schütt, M. Strange, K.S. Thygesen, T. Vegge, L. Vilhelmsen, M. Walter, Z. Zeng, K.W. Jacobsen, The atomic simulation environment-a python library for working with atoms, J. Phys.: Condens. Matter 29 (27) (2017) 273002URL: http://stacks.iop.org/0953-8984/29/i=27/a=273002.

[76] F. Birch, Elasticity and constitution of the earth's interior, J. Geophys. Res. 57 (2) (1952) 227–286, https://doi.org/10.1029/JZ057i002p00227 arXiv: https://agupubs.onlinelibrary.wiley.com/doi/pdf/10.1029/JZ057i002p00227 ,https://agupubs.onlinelibrary.wiley.com/doi/abs/10.1029/JZ057i002p00227.

[77] D.H. Chung, W.R. Buessem, The voigt reuss hill approximation and elastic moduli of polycrystalline MgO, CaF$_2$, ZnS, ZnSe, and CdTe, J. Appl. Phys. 38 (6) (1967) 2535–2540, https://doi.org/10.1063/1.1709944.

[78] W.-J. Ding, J.-X. Yi, P. Chen, D.-L. Li, L.-M. Peng, B.-Y. Tang, Elastic properties and electronic structures of typical al-ce structures from first-principles calculations, Solid State Sci. 14 (5) (2012) 555–561, https://doi.org/10.1016/j.solidstatesciences.2012.02.006 URL: http://www.sciencedirect.com/science/article/pii/S1293255812000581.

[79] D. Alfe, Comput. Phys. Commun. 180 (2009) 2622.

[80] D. Schumacher, A. Seeger, O. Harlen, Vacancies, divacancies, and self-diffusion in platinum, Phys. Stat. Sol. 25 (1968) 359.

[81] G.L. Bacchella, E. Germagnoli, S. Granata, On the kinetics of quenched-in lattice vacancies in platinum, J. App. Phys. 30.

[82] W. Hertz, H. Peisl, Volume and electrical resistivity change due to vacancies in platinum, J. Phys. F: Metal Phys. 5 (1975) 604.

[83] X. Zhang, G. Lu, Electronic origin of void formation in fcc metals, Phys. Rev. B 77 (2008) 174102.

[84] P.A. Korzhavyi, I.A. Abrikosov, B. Johansson, First-principles calculations of the vacancy formation energy in transition and noble metals, Phys. Rev. B 59 (1999) 11693.

[85] V.K. La Mer, Jour. Chem. Phys. 1 (1933) 289.

[86] S.W. Benson, Thermochemical kinetics: methods for the estimation of thermochemical data and rate parameters, second ed., Wiley, New York.

[87] A. Stroppa, G. Kresse, New J. Phys. 10 (6) (2008) 063020, , https://doi.org/10.1088/1367-2630/10/6/063020 https://doi.org/10.1088.

[88] J. Boes, J. Kitchen, Neural network predictions of oxygen interactions on a dynamic Pd surface, Mol. Simulat. 43 (5) (2017) 346–354, https://doi.org/10.1080/08927022.2016.1274984.

[89] J. Byggmästar, A. Hamedani, K. Nordlund, F. Djurabekova, Machine-learning interatomic potential for radiation damage and defects in tungsten, Phys. Rev. B 100 (14) (2019) 144105, https://doi.org/10.1103/PhysRevB.100.144105.